Title

Long-Range Exciton Diffusion in Two-Dimensional Assemblies of Cesium Lead Bromide Perovskite Nanocrystals

Journal

ACS Nano, 14(6)

ISSN

1936-0851

Authors

Penzo, Erika

Loiudice, Anna

Barnard, Edward S

et al.

Publication Date

2020-06-23

DOI

10.1021/acsnano.0c01536

Peer reviewed

Long-Range Exciton Diffusion in Two-Dimensional Assemblies of Cesium Lead Bromide Perovskite Nanocrystals

Erika Penzo,* Anna Loiudice, Edward S. Barnard, Nicholas J. Borys, Matthew J. Jurow, Monica Lorenzon, Igor Rajzbaum, Edward K. Wong, Yi Liu, Adam M. Schwartzberg, Stefano Cabrini, Stephen Whitelam, Raffaella Buonsanti, and Alexander Weber-Bargioni*

ABSTRACT: Förster resonant energy transfer (FRET)-mediated exciton diffusion through artificial nanoscale building block assemblies could be used as an optoelectronic design element to transport energy. However, so far, nanocrystal (NC) systems supported only diffusion lengths of 30 nm, which are too small to be useful in devices. Here, we demonstrate a FRET-mediated exciton diffusion length of 200 nm with 0.5 cm^2/s diffusivity through an ordered, two-dimensional assembly of cesium lead bromide perovskite nanocrystals ($CsPbBr_3$ PNCs). Exciton diffusion was directly measured *via* steady-state and time-resolved photoluminescence (PL) microscopy, with physical modeling providing deeper insight into the transport process. This exceptionally efficient exciton transport is facilitated by PNCs' high PL quantum yield, large absorption cross section, and high polarizability, together with minimal energetic and geometric disorder of the assembly. This FRET-mediated exciton diffusion length matches perovskites' optical absorption depth, thus enabling the design of device architectures with improved performances and providing insight into the high conversion efficiencies of PNC-based optoelectronic devices.

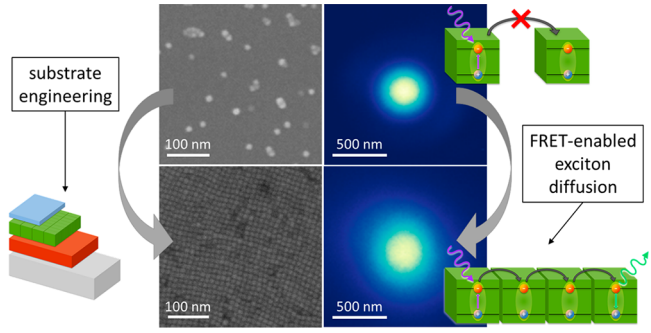

Energy transport at the nanoscale plays a critical role in a plethora of natural systems: for instance, the photo-synthetic process relies on Förster resonant energy transfer (FRET) to transport energy along a few μm of diffusion length[1] as well as to be the primary mechanism of energy transport between proteins or different moieties of the same protein.[2] A detailed understanding of the FRET mechanism is pivotal to the realization of artificial systems with efficient, long-range energy propagation.

Quantum dot (QD) solids have recently gained a lot of attention, thanks to the advantages of engineering 3D arrays with nanoscale building blocks. QDs are well-known for their exceptional optical properties as well as for the possibility to easily tune such properties by changing their size, composition, and surface chemistry.[3−5] In addition, their self-assembly in close-packed systems facilitates the communication between neighboring QDs, by enabling FRET of excitons that are able to hop onto adjacent, nonexcited QDs, which results in the transport of the excitonic energy for multiple steps before the exciton recombines. Understanding FRET-mediated exciton diffusion is critical for enhancing the performances of optoelectronic devices, such as flexible organic light-emitting diodes (OLEDs), solar cells, and light modulators,[6] by engineering the diffusion appropriately for the desired application. For instance, solar cells largely benefit from the migration of excitons toward the charge-separation interfaces.[5,7] Conversely, in light-emitting devices, a large diffusion of excitons is detrimental to the efficiency, since it prevents the exciton from radiatively emitting from the QD where it formed, thus risking its nonradiative trapping onto adjacent layers.[5,7] Artificial nanoscale building block assemblies are characterized by relatively short FRET-mediated exciton diffusion lengths, typically on the order of 10 nm in organic

semiconductors,[8] 30 nm in inorganic nanocrystal (NC) solids,[9] and up to 50−70 nm in perovskite nanocrystal (PNC) assemblies,[10] which is a major limitation to the exploration of exciton-based optoelectronic phenomena and to the development of optoelectronic devices. Here, we show that, within close-packed, two-dimensional assemblies of isoenergetic PNCs, FRET-mediated exciton diffusion lengths reach 200 nm, close to the light absorption depth of 200−400 nm for this class of materials,[11] and the so far longest reported FRET-mediated exciton diffusion length in a NC system.

The Förster equation describes the structural and optoelectronic requirements between a donor−acceptor system to maximize the FRET rate:[12]

$$1/\tau_{DA} = \frac{2\pi}{\hbar}\frac{\mu_D^2\mu_A^2\kappa^2}{r_{DA}^6 n^4}$$

$1/\tau_{DA}$ is the hopping rate between a donor (D) particle and acceptor (A) particle with τ_{DA} being the average time for an exciton to hop from a donor to an acceptor. Maximizing this hopping rate requires (1) minimizing interparticle distances r and the refractive index n, (2) maximizing the spectral overlap between donors and acceptors $\mu_D^2\mu_A^2$, and (3) aligning the dipole moments to maximize the orientation factor k.[2] Additional parameters critical to experimentally study the transport are maximizing the polarizability of individual emitters to enhance (4) photon absorption and hence exciton creation, (5) the fluorescent quantum yield for an optimized signal-to-noise ratio, and (6) a flat energy landscape between the particles (small inhomogeneous line broadening). Importantly, these six parameters affect the exciton diffusion multiplicatively, meaning that if one parameter is poorly optimized, exciton diffusion can be completely suppressed. Hence, most studies of exciton transport through nanoscale building block assemblies find an exciton diffusion length of 6−30 nm (diffusion coefficient of 0.2−12 × 10^{-3} cm^2/s) for chalcogen-based quantum dot (QD) assemblies[7,9,13] and a length of 3−50 nm for organic systems where the exciton transport occurs *via* singlet emitters and therefore FRET.[14−17] The short diffusion lengths are attributed to one or several of these parameters to be limiting, for instance, the spatial disorder in QD assemblies.

PNCs are a fascinating NC class with the potential to excel in all of these parameters. As bulk semiconductors, lead halide perovskites have emerged as a promising class of materials for low-cost, solution-processable optoelectronics,[18−21] demonstrating thin-film solar cell power conversion efficiencies exceeding 25%[22,23] and LEDs with 20% external quantum efficiency.[24−27] In the form of NCs, the all-inorganic cesium lead halide ($CsPbX_3$, X = I, Br, or Cl) PNCs provide high optical tunability as a function of composition,[28−31] size,[30,32−35] and shape,[32,33,36] with impressive exciton generation efficiency[37] and scalable solution-phase processes.[38−41] Although the quantitative use of the FRET equation is beyond the scope of this work, we note that in terms of FRET-mediated transport, the PNCs qualitatively optimize all six parameters: (1) The interparticle distance r is determined by the ligand (oleic acid and oleylamine) and amounts to 2 nm. (2) The spectral overlap is high due to narrow emission line widths and small Stokes shifts.[28] Furthermore, their defect-tolerant optical emission (responsible for record efficiencies in QD solar cells)[29] maintains the symmetric and narrow emission bands compared to chalcogen-based NCs[21] and, hence, the high spectral overlap. The transition dipoles (3) between adjacent PNCs have been reported to be well-aligned as well,[42] due to their cubic shape directing the overall orientation in a self-assembled layer. PNCs have also demonstrated a combination of high photon absorption crosssection (4) and near-unity quantum yield (5).[43] A flat energy landscape (6) among NCs can be obtained by controlling the NC size in a weakly quantum confined regime where the energy bandgap is primarily determined by the chemical composition so as to reduce the thermalization of excitons toward NCs with a smaller bandgap, which would limit the back transfer onto larger bandgap NCs and therefore decrease the sites' availability for the exciton random hopping.[28]

In this work, we show that indeed, FRET-mediated exciton transport through self-assembled close-packed PNC monolayers reaches over 200 nm with a diffusivity of ∼0.1 cm^2/s, which is in terms of diffusion length 1 order of magnitude higher and in terms of diffusivity 2 orders of magnitude larger than previously reported for chalcogen-based QDs.[9] We demonstrated these values by studying the exciton diffusion in a close-packed monolayer of $CsPbBr_3$ PNCs. Importantly, in order to create a model system for the study of such diffusion, we took particular care in the sample preparation and developed a strategy to deposit only one monolayer of PNCs per sample. The ordered self-assembly of PNCs in a monolayer causes the exciton propagation to be restricted to two dimensions only, allowing us to directly image the exciton motion on a 2D plane without any loss of data in the third dimension. Moreover, this 2D PNC assembly can be replicated theoretically with a 2D random walk, thus simplifying the interpretation of experimental data within a statistic framework. The diffusion length and the diffusivity were determined *via* steady-state photoluminescence (PL) microscopy mapping and time-resolved PL mapping, respectively. The diffusion was modeled using continuum and discrete representations of exciton hopping to provide a physical interpretation of our experiments, showing that albeit demonstrating a record FRET-mediated exciton diffusion length, our system is still in a subdiffusive regime.

DISCUSSION

To simplify the direct visualization of exciton transport, we confined the PNCs in a self-assembled monolayer on a Si wafer with about 1 nm of native oxide and coated with ∼10 nm of a hydrocarbon polymer, deposited *via* plasma polymerization of methane, to prevent both exciton quenching into the Si and wave-guiding along the dielectric layer. We made two kinds of samples, a close-packed sample to study the exciton diffusion and a control sample with a sparse layer of small groups of PNCs separated by at least 20 nm to prevent FRET-based diffusion. The NCs examined in this study were cubic $CsPbBr_3$ PNCs with an average side length of 10 nm, synthesized according to an established procedure.[28] Spin-coating from a toluene solution on a surface functionalized with a −CH terminated polymer reproducibly yielded close-packed monolayers with an interparticle spacing of ∼2 nm, which is determined by the ligand length (see Figure 1, Methods, and the SI for a detailed description of the sample preparation methods). In order to stabilize the PNCs during optical characterization (conducted at room temperature and under ambient atmosphere), we adapted a recently reported passivation process:[44] after spin-coating the solution of

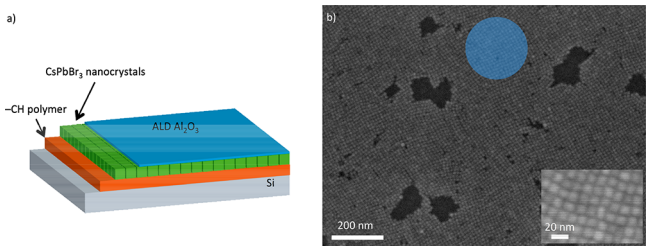

Figure 1. Deposition of controlled PNC 2D architectures. (a) $CsPbBr_3$ PNCs in toluene were spin-coated onto a Si substrate functionalized with a −CH terminated polymer and coated with 3 nm of aluminum oxide deposited by ALD to prevent degradation during measurements. (b) Scanning electron microscopy (SEM) micrograph of a close-packed monolayer of PNCs. The blue circle shows the size (fwhm ∼200 nm) of the excitation laser spot used in subsequent optical experiments.

PNCs, we deposited ∼3 nm of aluminum oxide by plasma-assisted atomic layer deposition (ALD). The passivated samples emitted stable PL upon illumination with continuous wave (CW) laser powers as high as 2000 W/cm^2 or with pulsed laser fluences as high as 50 μJ/cm^2.

Exciton diffusion in NC solids and organic semiconductors has predominantly been studied indirectly by spectroscopic techniques, which can only provide a coarse estimate of the diffusion length.[7,45] Recent microscopy-based approaches allow for the direct measurement of diffusion dynamics including the two main quantities that characterize exciton diffusion: the diffusion length and the diffusion coefficient (or diffusivity).[9]

Figure 2 illustrates the basic principles of the visualization of exciton diffusion. In order to measure the diffusion length and coefficient, we start by exposing the PNC monolayer to a perpendicular laser beam, whose size is kept as close as possible to the diffraction limit. The laser beam generates a local population of excited states in the PNC monolayer, with an initial spatial distribution that matches the intensity profile of the excitation spot. The PL maps were recorded with a CCD camera, after sample excitation with a 450 nm laser, whose spot was kept as close as possible to the diffraction limit, with an fwhm of 240 nm (Supplementary Figure S18). If the motion of an exciton is allowed, for instance, by FRET-induced hopping onto a nearby PNC, then it is possible that such an exciton will travel before radiatively recombining. Our sample preparation greatly enhances the probability of such hopping by promoting the self-assembly of the PNCs in a close-packed monolayer. Excitons can therefore propagate within the 2D plane of the monolayer, which ultimately results in a radial expansion from the excited-state distribution (Figure 2a) and in a broader spot of the collected PL with respect to the excitation spot. Conversely, if the distance increases with respect to the close-packed case, the FRET hopping is not allowed, and the emission can only occur from the same PNC that was initially excited (Figure 2b). In order to better understand this effect, we report in Figure 2b,c two images of PNCs, one in a close-packed lattice and the other one when the PNCs are spin-coated onto a nonengineered substrate, thus resulting in a random distribution where each PNC is far enough from others (at least 20 nm) to hinder FRET transport. The collected PL from such samples is reported in Figure 2e,f. Here, we can appreciate the significantly different results of the excitation with the same spot, shape, and energy: the spatial

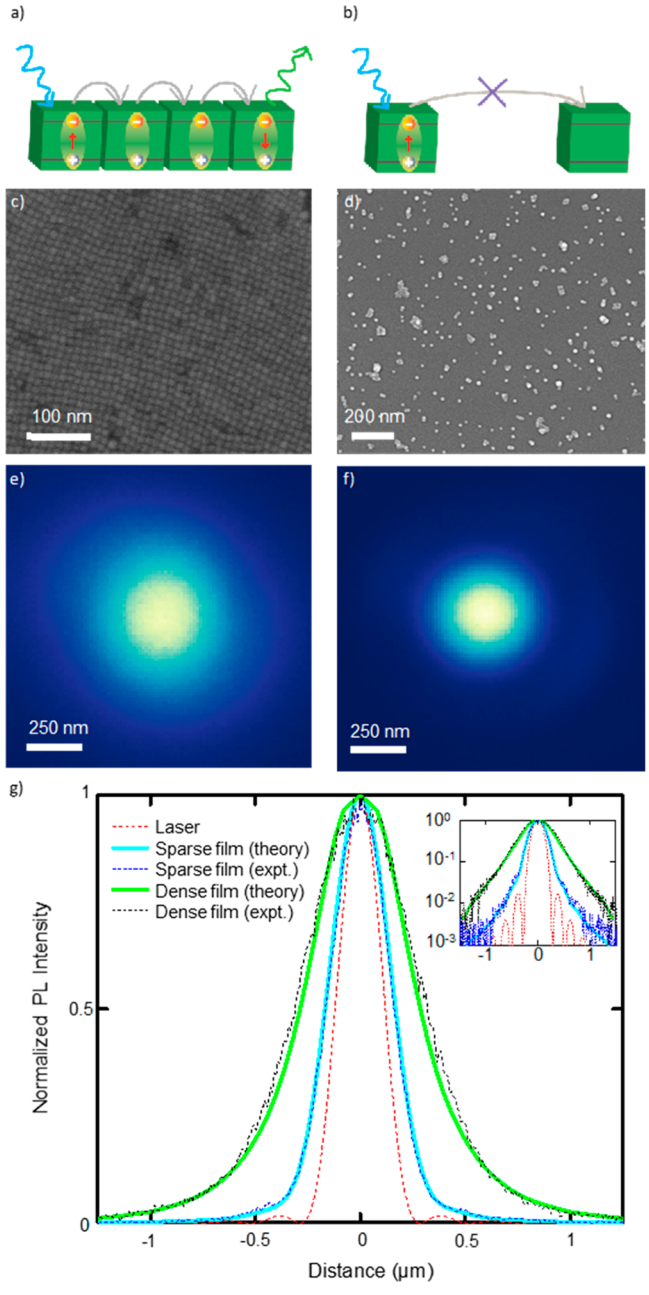

Figure 2. Direct measurement of steady-state exciton diffusion. (a) When PNCs are assembled in a close-packed monolayer, the distance between NCs is minimized, allowing for efficient FRET-mediated exciton diffusion. (b) When PNCs are spatially separated, FRET-mediated exciton diffusion is inhibited. (c) SEM micrograph of a close-packed monolayer of PNCs. (d) SEM micrograph of a sparse monolayer of PNCs. (e) Normalized PL intensity profile emitted by the close-packed PNC monolayer when excited with a diffraction-limited laser spot with a wavelength of 450 nm. (f) Normalized PL intensity profile emitted by the sparse PNC monolayer when excited with a diffraction-limited laser spot with a wavelength of 450 nm. (g) PL profile cross sections of panel (e) (black dashed line) and (f) (blue dashed line) together with simulated PL profile cross sections for a square lattice of nanoparticles with a vacancy fraction of 20% (green line) and for a sparse sample of nanoparticles on which hopping cannot occur (cyan line). The dashed red line corresponds to the excitation laser profile cross section. The inset shows the main figure on a logarithmic vertical scale.

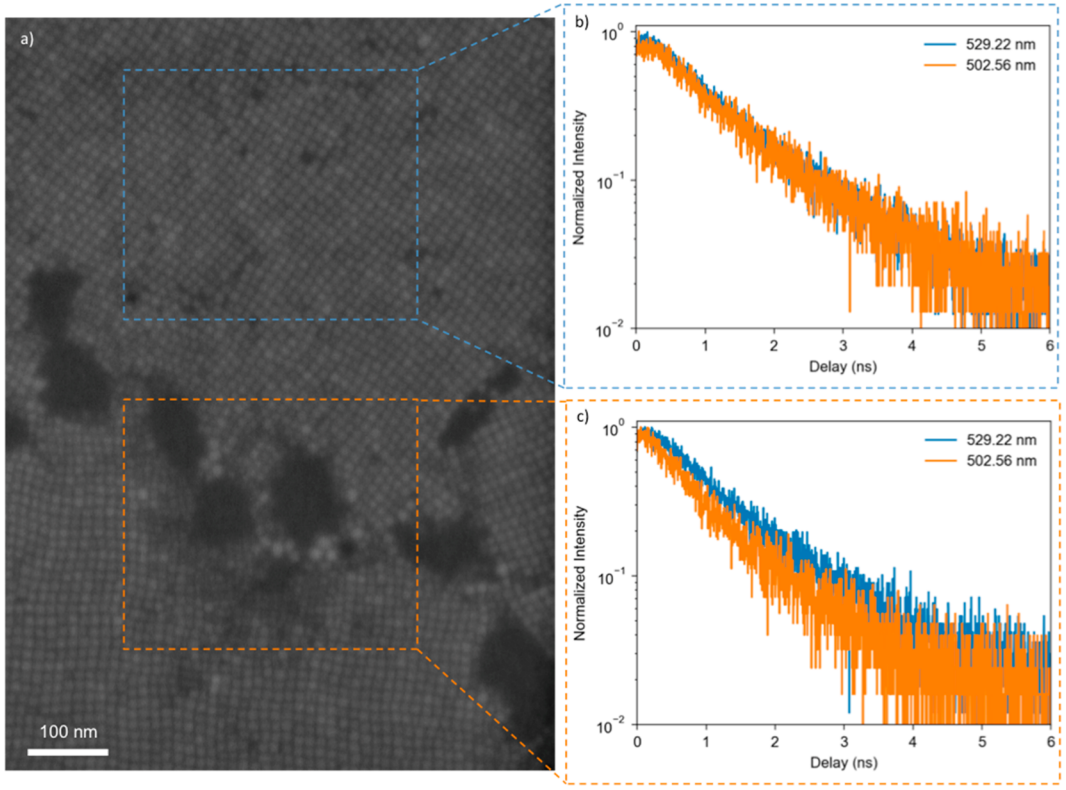

Figure 3. Probing the energy landscape by time-resolved PL spectroscopy. (a) SEM micrograph of a close-packed monolayer of PNCs showing ordered areas made of uniformly sized PNCs (blue dashed rectangle) and disordered areas made of PNCs of different sizes at a crack in the film (orange dashed rectangle). (b) PL intensity as a function of time at two emission wavelengths, 529.22 nm (blue solid line) and 500.56 nm (orange solid line), measured on an ordered area made of uniformly sized PNCs. The overlap of the curves indicates equivalent PL lifetimes at both emission wavelengths. (c) PL intensity as a function of time at two emission wavelengths, 529.22 nm (blue solid line) and 500.56 nm (orange solid line), measured on a disordered area made of PNCs of different sizes. The orange curve displays the slower decay of the low-energy portion of the PL spectrum, due to exciton migration to smaller bandgap PNCs.

extent of the PL map collected from the close-packed sample is much broader than the excitation spot, whereas in the sample in which excitons cannot hop the spatial extent of the PL map resembles the excitation spot, only slightly enlarged due to the convolution of the point-spread function of the microscope with the spatial profile of the excitation spot (*i.e.*, a convolution of a diffraction-limited point source with the diffraction-limited spot of a focused laser beam; see Supplementary Figure S18). A schematic of the setup is shown in Supplementary Figure S19. In order to provide a more quantitative comparison between the two images, in Figure 2g we report a line scan through both PL maps as extracted from Figure 2e,f. Both spots are radially symmetric, so we can take any direction in each spot and compare their relative cross sections. In a first order approximation, it is possible to describe the diffusion profile within a Gaussian framework. By subtracting the variances of the Gaussian fits with and without diffusion (close-packed vs sparse monolayer), we obtain a first estimate of the diffusion length, as explained in detail in the Supporting Information (see Section S2). In order to provide a theoretical support for our data, we perform a detailed set of calculations, which are reported in the Supporting Information (see Sections S3–S6). Specifically, we model the steady-state diffusion using two complementary approaches, namely, (i) continuum equations (S4) and (ii) microscopic simulations (S5). First, we approximate the processes of creation, hopping, and recombination of optically excited excitons in nanoparticles by considering the statistic of classical bosonic particles on a lattice, in steady-state conditions. This description results in the derivation of a continuity equation, where the concentration of excitons is the physical quantity that undergoes a spatial variation with its own diffusion constant. The equation is solved both numerically and semianalytically, with agreement between the two solutions in the linear regime, *i.e.*, the condition of low excitation power in which the optical measurements were conducted. The semianalytic solution is particularly useful to simulate the trends in nonlinear regimes, that is, when the excitation power is large enough to prompt a power-induced change of the exciton diffusion profile. The modeling *via* the continuity equation ultimately indicates that our PL profiles are consistent with a mean excitonic diffusion constant of the order of 0.5 cm^2/s, or $(224\ nm)^2/ns$, which results in a characteristic exciton diffusion length of about 200 nm (consistent with the simple estimate in which we approximate profiles as Gaussian distributions).

In addition, we perform a set of discrete-time and continuous-time Monte Carlo simulations, where we model excitons as classical particles, able to undergo various processes, sitting with fixed positions within a 2D square array, similarly to the experimental sample. Using a model that assumes a completely uniform film of NCs, subtle but significant variations occur between the tails of measured and predicted profiles. However, as seen in the SEM images, vacancies occur in the experimental film (Figure 1b). These vacancies can inhibit further exciton propagation. Hence, in

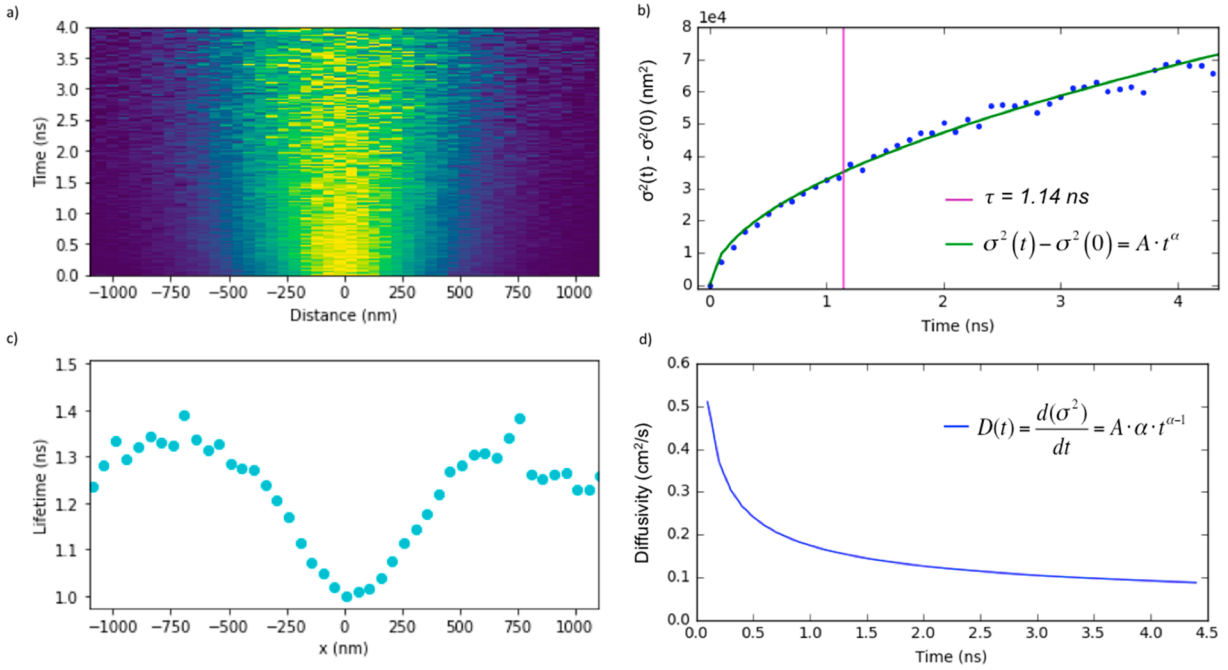

Figure 4. Probing exciton diffusion dynamics by time-resolved optical microscopy. (a) Time evolution of cross-sectional PL intensity profile. (b) PL profile variance increase as a function of time (blue dots). The green solid line shows the fit to the power law $A{\cdot}t^{\alpha}$ (A = 0.3527 cm^2/s, α = 0.53). (c) Space-resolved PL lifetime calculated from the signal in (a) as the time for 37% or 1/e decay of PL intensity. (d) Diffusivity (or diffusion coefficient) as a function of time calculated as the first derivative of the PL profile variance variation in (c).

order to provide a more realistic description of our system, we carry out Monte Carlo simulations in the presence of both spatial and energetic disorder. Spatial disorder is taken into account by arranging the available sites in a non-close-packed fashion, so that the hopping of an exciton onto a neighbor PNC may be inhibited due to excessive distance from the closest neighbor, whereas energetic disorder takes into account the deviation from perfectly isoenergetic particles and hence the presence of larger or smaller PNCs, resulting in (slightly) smaller or larger bandgap energies. When such disordered conditions are included in the model, the predicted PL profiles reproduce the experimental PL profile more closely (Figure 2g).

Importantly, the excitation power in all measurements was kept sufficiently low so as to remain in the linear excitation regime (see Methods and Supplementary Figure S23). The presented interpretation of deconvolving the Gaussian distributions and extracting the diffusion lengths is only correct in the regime where PL intensity scales linearly with the excitation power. At higher pump fluences, exciton−exciton annihilation starts taking place, thus introducing an additional term in the diffusion equations that may lead to significantly broader PL profiles that could be interpreted as enhanced exciton diffusion, while actually, it is related to a steep exciton concentration gradient, and the effective diffusion length for each exciton is still the same. A detailed discussion is reported in the Supporting Information.

$CsPbBr_3$ PNCs are not strongly quantum confined in the size range used in this study (10 nm average cube side);[28] as a result, our close-packed monolayers mostly constitute a flat energy landscape for exciton diffusion, which is a requirement to maximize FRET in a NC solid. In the presence of energetic heterogeneity, excitons travel downhill in energy and thermalize onto NCs with smaller bandgaps. The process of back transfer onto larger bandgap energies has a lower rate and is less likely to take place, thus limiting the availability of viable neighbors for an exciton to hop on. Because of this more efficient funneling of excitons from high-energy to low-energy states than vice versa, signatures of this inhomogeneity-driven process can be discerned in the temporal evolution of the PL spectrum after pulsed excitation. The additional energy transfer relaxation channels of the high-energy sites accelerate their relaxation rates, yielding energy-dependent excited-state lifetimes, where higher-energy NCs have shorter lifetimes than those with lower energies. Thus, following pulsed excitation, the PL spectrum typically shifts to lower energies as the higher-energy NCs relax more rapidly than the lower-energy NCs. Experimentally, this behavior can be resolved as time-dependent shifts in the PL spectrum to lower energy or emission-energy-dependent relaxation kinetics. In colloidal semiconducting NCs, this energetic heterogeneity largely arises from the polydispersity of the sample where the larger quantum dots are less quantum confined, have lower-energy excited states, and thus serve as sites where an exciton can easily transfer to but from where it cannot easily leave.[46,47]

In Figure 3, we used time-resolved PL (TRPL) spectroscopy to assess the disorder in the energetic landscape in our films. As shown in Figure 3a, during the assembly process, energy minimization pushes the PNCs of different sizes to the edges of the ordered, close-packed regions. The result is that the central regions of the film are significantly less polydisperse than the edges. Examples of a uniform area (top dashed rectangle) and of a nonuniform area (bottom dashed rectangle) are highlighted in Figure 3a. As seen in Figures 1b and 2c, the exciton diffusion studies were performed in the regions with monodisperse PNCs; in these portions of the film, time-resolved PL spectroscopy measurements displayed identical decay kinetics for the high- and low-energy components of the PL spectrum (Figure 3b), and accordingly, the PL spectrum does not change with time (Supplementary

Figure S20). In contrast, in the edge regions with maximal polydispersity, signatures of excitons getting funneled in lower-energy bandgap NCs were subtle but detectable: the lower-energy emission (2 nm band; centered at 529.2 nm) decays slower than the higher-energy emission (2 nm band; centered at 502.6 nm), and the PL spectrum exhibits a clear evolution to lower energies following pulsed excitation (Supplementary Figure S20). These results indicate that within the central regions of the film the site-to-site variations in energy are minimized, thus strongly reducing, or possibly eliminating, exciton funneling toward low-energy sites. Therefore, only at the edges, where the polydispersity is maximal, we see evidence of an energetic landscape where the energy transfer toward smaller bandgap NCs is more efficient. Rather, in the central regions, the weak quantum confinement combined with the assembly process play a pivotal role in achieving the long exciton diffusion distance. Future work will be dedicated to a detailed investigation of the redshift observed in defectual areas.

To better understand and measure the dynamics of the long-distance exciton diffusion, time-resolved PL microscopy was employed to track the temporal evolution of the PL spatial profile as it expanded from its initial state. Areas of the close-packed monolayer of monodisperse PNCs were excited with short laser pulses, and the magnified PL emission (100×) was collected by a single-mode fiber (with a diameter of 5 μm). To gain spatial resolution, the collection fiber was mounted on a translation stage that systematically scanned the fiber aperture in the focal plane of the microscope. At each fiber position, a full time-resolved PL transient was recorded, which allowed us to track how the excited state expanded with time. The temporal evolution of the normalized PL profile is shown in Figure 4a, where the 0 nm distance corresponds to the position of the fiber, which is aligned with the center of the PL spot. Distances greater than zero are reported as the distance between the center of the PL spot and the center of the image of the fiber aperture on the sample plane. The spatially and time-resolved PL trace in Figure 4a clearly displays the expected diffusive broadening, which can be quantified by calculating the PL profile width at each time slice (Figure 4b). The rate at which the variance of the spatial PL profile (Gaussian fit) rises with time is sublinear, indicating a subdiffusive process, which, as discussed above, is very likely due to PNC voids in the film. In these dynamic measurements, as reported in previous work,[9] the average exciton diffusion length is calculated as the increase in the PL profile variance from its initial state (right after excitation) to the average lifetime of the system. The average lifetime of these PNCs in a close-packed film is 1.14 ns (as calculated as the time to reach a decay of 37% or $1/e$ of the PL intensity, see Supplementary Figure S21), which, using the dynamics in Figure 4b, yields an average exciton diffusion length of 194 nm that is in very good agreement with that derived from our steady-state measurements.

The PL lifetime was also calculated at each point (a PL lifetime map is shown in Supplementary Figure S22) and was observed to decrease as the reciprocal of the PL intensity (Figure 4c). This spatially dependent change in dynamics is an expected effect of the diffusion process, which is driven by the exciton density gradient, and results in a larger net outward exciton flux in areas with a large exciton population. The minimum lifetime was found to be 1 ns and grew to 1.3 ns 500 nm away from the excitation intensity maximum. The majority of the signal (>90%) lies between −500 and 500 nm from the excitation maximum; as a result, the lifetimes calculated for values ≤750 and >750 nm are very scattered, since the diffusion outside this region is almost completely exhausted, and the signal is weak and indistinguishable from noise (especially considering that we are collecting with a single-mode fiber with a diameter of 5 μm). Importantly, we highlight that the measurements were performed with excitation intensities that are deep in the linear regime of the power-dependence of the PL (see Supplementary Figure S23); therefore, we exclude the possibility that the central decrease in lifetime is due to higher-order nonradiative recombination processes (*e.g.*, Auger recombination).

The diffusion coefficient (or diffusivity) was calculated as the first derivative of the PL profile variance increase in time and is shown in Figure 4d. The effective diffusivity was found to decrease with time, from 0.5 cm^2/s right after excitation to ∼0.1 cm^2/s at the end of the diffusion process.

These values of FRET-mediated exciton diffusion length and diffusivity are the largest reported so far for NC solids. Chalcogen-based QDs demonstrated diffusion lengths in the range of 20−30 nm and diffusivities between 0.2×10^{-3} and 1.5×10^{-3} cm^2/s.[9] The system here reported demonstrated a 1 order of magnitude higher diffusion length and about 2 orders of magnitude higher diffusivity. Significantly, the exciton diffusion dynamics in our PNC films is comparable with the dynamics of unbound charge carriers in other bulk perovskite materials. Individual crystals of a $CsPbI_2Br$ perovskite measured by pump−probe microscopy revealed a diffusivity of 0.27 cm^2/s,[48] and thin films of polycrystalline hybrid perovskite measured by transient absorption microscopy showed a diffusivity in the range of 0.05 to 0.08 cm^2/s, with diffusion lengths of 220 nm in the 2 ns experiment time.[49]

CONCLUSIONS

In conclusion, ordered monolayers of isoenergetic PNCs were fabricated *via* controlled self-assembly. This system demonstrated extremely efficient FRET-mediated exciton diffusion, which was directly characterized by steady-state and time-resolved PL microscopy together with an analytical and statistical model that granted a deeper understanding of the exciton diffusion dynamics. Our measurements directly capture a diffusion length of 200 nm and a diffusivity of 0.5 cm^2/s. This diffusion length is 10 times longer and the diffusivity is 2 orders of magnitude larger than previously reported values for films of chalcogen-based QDs[9,50] and comparable to those of charge-carrier diffusion in thin films of polycrystalline hybrid perovskites. Demonstrating such long-range diffusion, our PNC system is ideally suited to study FRET processes and FRET-mediated energy transfer on length scales that are easily accessible and therefore easy to optimize. Moreover, long exciton diffusion establishes an additional design element for next generation PNC-based optoelectronic devices.[21,51]

Further progress toward even longer-range exciton diffusion may be achieved by improving PNCs' energetic uniformity as well as by optimizing the protective ALD-based process that prevents perovskite degradation. Additionally, fabricating PNC assemblies with increased complexity, for example, deliberately varying interparticle distance in certain assembly portions or by positioning PNCs with decreasing bandgap next to each other forming an oriented energy funnel, could demonstrate ways to move excitons to predetermined positions. Overall, we showed that ordered assemblies of isoenergetic PNCs support FRET-

mediated exciton diffusion with exceptional lengths, which can be used to better the performances of PNC-based optoelectronic devices.

METHODS

PNC Synthesis and Characterization. $CsPbBr_3$ nanocubes were synthesized by a procedure adapted from the original report.[28] All chemicals were purchased from Sigma-Aldrich and used as received without further purification. Cs_2CO_3 (1.2 mmol) was added to 10 mL of 1-octadecene and stirred at 120 °C under vacuum for 1 h. Oleic acid (2 mmol) was injected under a nitrogen atmosphere, and the resulting mixture was stirred at 120 °C for 2 h until fully dissolved. In a separate container, $PbBr_2$ (0.19 mmol) was added to 5 mL of 1-octadecene and stirred at 120 °C under vacuum for 1 h. Oleic acid (1.6 mmol) and oleylamine (1.5 mmol) were injected under a nitrogen atmosphere. The resulting mixture was stirred at 120 °C for 2 h until fully dissolved and then was heated to 165 °C. To this preheated lead solution was added 0.4 mL of hot Cs_2CO_3 solution under a nitrogen atmosphere with vigorous stirring. The reaction was stirred for 5 s and cooled rapidly in an ice bath until the reaction mixture solidified. After freezing, the reaction mixture was warmed to room temperature and transferred into centrifuge tubes. The mixture was centrifuged at 8500 rpm, for 10 min. The supernatant was discarded, and the pellet was redispersed in anhydrous hexane (6 mL). An equal volume of *tert*-butanol was added to precipitate the NCs, and the mixture was centrifuged at 12 000 rpm for 15 min. The supernatant was discarded, and the pellet was redispersed in toluene. These solutions were then centrifuged for 5 min at 700 rpm, and the pellet was discarded to remove large aggregates. The supernatant was transferred to a glovebox for film deposition.

PNC Monolayer Fabrication. PNCs monolayers were prepared by spin coating (1500 rpm, 45 s) from a colloidal suspension of nanocubes in toluene onto Si wafers coated with 10 nm of a −CH terminated polymer, which is sufficiently thin to prevent lateral waveguiding but thick enough to prevent exciton quenching by the silicon. The concentration was 3 g/L for the close-packed monolayer and 60 mg/L for the sparse monolayer. The hydrocarbon polymer was deposited by polymerizing methane in a plasma chamber (40 mTorr, RF power 100 W, 10 °C, Oxford Instruments). Aluminum oxide (3 nm) was deposited by plasma-assisted atomic layer deposition at 40 °C (Oxford Instruments). Films were characterized by SEM (Zeiss).

Steady-State PL Microscopy. The setup for steady-state PL microscopy is shown in Supplementary Figure S3a. The 450 nm CW diode laser source was collimated and then focused to a diffraction-limited spot by a 100× 0.95 NA objective lens. The back aperture of the objective was overfilled to ensure diffraction-limited performance. Emission from the sample was collected by the same objective and additionally magnified 5.3× for a total magnification of 530× and imaged on a CCD camera (QSI SI 660 6.1mp Cooled CCD Camera) with a pixel size of 4.54 μm, which provided an effective imaging pixel size of 8.63 nm. A 490 nm long-pass dichroic filter (Semrock Di03-R488-t1) and two 496 nm long-pass edge filters (Semrock) were used to remove the excitation laser beam from the PL signal. The laser beam was imaged through the 490 nm long-pass dichroic filter (Semrock) and a 498 nm short-pass edge filter (Semrock) to remove the PL signal. Measurements were performed at 45 W/cm^2, which corresponds to the probability of one absorbed photon per 1705 nanocubes during the 1.15 ns average lifetime.

Time-Resolved PL Spectroscopy. The setup for time-resolved PL microscopy is shown in Supplementary Figure S3b. The pulsed laser source (center wavelength 465 nm with a 2.5 nm bandwidth; 5 ps pulse duration; 40 MHz repetition rate) was collimated and focused by a 100× 0.95 NA objective lens. The back aperture of the objective was overfilled to ensure diffraction-limited performance. Emission from the sample was collected by the same objective. A 490 nm long-pass dichroic filter (Semrock) and a 496 nm long-pass edge filter (Semrock) were used to remove the excitation laser beam from the PL signal. The PL spectral components were separated with a monochromator (Princeton Instruments Acton 2300i) and detected by a single-photon counting avalanche photodiode (MPD PDM series) connected to a time-correlated single-photon counting unit (Picoharp 300). The temporal resolution was approximately 50 ps as determined by the fwhm of the instrument response function.

Measurements were performed at a laser fluence of 2.5 μJ/cm^2, which corresponds to the average probability of 1 absorbed photon per 32 nanocubes per pulse.

Time-Resolved PL Microscopy. The setup for time-resolved PL microscopy is shown in Supplementary Figure S3c. The pulsed laser source (center wavelength 465 nm with a 2.5 nm bandwidth; 5 ps pulse duration; 40 MHz repetition rate) was collimated and focused by a 100× 0.95 NA objective lens. The back aperture of the objective was overfilled to ensure diffraction-limited performance. Emission from the sample was collected by the same objective and imaged on a single-mode fiber (P1-405P-FC-2, Thorlabs) attached to a translation stage (Attocube ECS series) that scanned the emission focal plane. The fiber mode field diameter was 2.5−3.4 μm at 480 nm; the stage was moved in 5 μm steps corresponding to 50 nm at the sample. A 490 nm long-pass dichroic filter (Semrock) and two 496 nm long-pass edge filters (Semrock) were used to remove the excitation laser beam from the PL signal. The laser beam was imaged through the 490 nm long-pass dichroic filter (Semrock) and a 498 nm short-pass edge filter (Semrock) to remove the PL signal. The signal was detected by a single-photon counting avalanche photodiode (MPD PDM-series) connected to a time-correlated single-photon counting unit (Picoharp 300). The temporal resolution was approximately 50 ps, as determined by the fwhm of the instrument response function.

Measurements were performed at a laser fluence of 5 μJ/cm^2, which corresponds to the average probability of 1 absorbed photon per 16 nanocubes per pulse.

The sample was mounted above the objective lens on a piezoelectric scanning stage. Samples were scanned during the course of the measurements (~30 min) over an area of 5 × 5 μm to avoid photobleaching or photodamage.

Physical Modeling. We simulated the processes of exciton creation, recombination, and hopping at continuum and microscopic levels of resolution. We convolved the resulting excitonic profiles with the optical point-spread function in order to calculate observed PL profiles. Full details of these calculations are given in SI Sections S3 to S6.

ASSOCIATED CONTENT

Supporting Information

The Supporting Information is available free of charge at https://pubs.acs.org/doi/10.1021/acsnano.0c01536.

Detailed description of the sample preparation and of the estimation of the diffusion length with a Gaussian approximation, a comprehensive section of the theoretical modeling *via* both continuity equations and Monte Carlo simulations, and supporting figures (PDF)

AUTHOR INFORMATION

Corresponding Authors

Erika Penzo − *The Molecular Foundry, Lawrence Berkeley National Laboratory, Berkeley, California 94720, United States*; Email: erikapenzo@gmail.com

Alexander Weber-Bargioni − *The Molecular Foundry, Lawrence Berkeley National Laboratory, Berkeley, California 94720, United States*; Email: awb@lbl.gov

Authors

Anna Loiudice − *Institute of Chemical Sciences and Engineering of the École Polytechnique Fédérale de Lausanne, Lausanne CH 1015, Switzerland*

Edward S. Barnard − *The Molecular Foundry, Lawrence Berkeley National Laboratory, Berkeley, California 94720, United States*
Nicholas J. Borys − *The Molecular Foundry, Lawrence Berkeley National Laboratory, Berkeley, California 94720, United States*
Matthew J. Jurow − *The Molecular Foundry and Materials Sciences Division, Lawrence Berkeley National Laboratory, Berkeley, California 94720, United States*
Monica Lorenzon − *The Molecular Foundry, Lawrence Berkeley National Laboratory, Berkeley, California 94720, United States;* orcid.org/0000-0003-3524-9546
Igor Rajzbaum − *The Molecular Foundry, Lawrence Berkeley National Laboratory, Berkeley, California 94720, United States*
Edward K. Wong − *The Molecular Foundry, Lawrence Berkeley National Laboratory, Berkeley, California 94720, United States*
Yi Liu − *The Molecular Foundry and Materials Sciences Division, Lawrence Berkeley National Laboratory, Berkeley, California 94720, United States;* orcid.org/0000-0002-3954-6102
Adam M. Schwartzberg − *The Molecular Foundry, Lawrence Berkeley National Laboratory, Berkeley, California 94720, United States*
Stefano Cabrini − *The Molecular Foundry, Lawrence Berkeley National Laboratory, Berkeley, California 94720, United States*
Stephen Whitelam − *The Molecular Foundry, Lawrence Berkeley National Laboratory, Berkeley, California 94720, United States*
Raffaella Buonsanti − *Institute of Chemical Sciences and Engineering of the École Polytechnique Fédérale de Lausanne, Lausanne CH 1015, Switzerland;* orcid.org/0000-0002-6592-1869

Author Contributions

The manuscript was written through contributions of all authors. R.B. and A.W.-B. conceived the initial work. A.L. and I.R. performed initial experiments. E.P. prepared the samples, conducted the diffusion experiments and analysis, and wrote the manuscript. S.W. developed theoretical modeling and analysis. A.L. and M.J.J. synthesized the nanocrystals with the supervision of R.B. and Y.L. E.S.B. and N.J.B. supported the experimental measurements and data analysis. E.P., E.K.W., and E.S.B. built the microscope. A.M.S. and S.C. supported the sample preparation and provided input into the data interpretation. E.P., E.S.B., N.J.B., M.J.J., A.M.S., S.W., M.L., and A.W.-B. helped with writing the manuscript. All authors have given approval to the final version of the manuscript.

Notes

The authors declare no competing financial interest.
A preprint version of this manuscript is deposited in arXiv: Erika Penzo; Anna Loiudice; Edward S. Barnard; Nicholas J. Borys; Matthew J. Jurow; Monica Lorenzon; Igor Rajzbaum; Edward K. Wong; Yi Liu; Adam M. Schwartzberg; Stefano Cabrini; Stephen Whitelam; Raffaella Buonsanti; Alexander Weber-Bargioni. Long-Range FRET-Mediated Exciton Diffusion in 2D Assemblies of $CsPbBr_3$ Perovskite Nanocrystals. *arXiv* 2020. arXiv: 2003.04353. https://arxiv.org/abs/2003.04353.

ACKNOWLEDGMENTS

This work was performed at the Molecular Foundry supported by the Office of Science, Office of Basic Energy Sciences, of the U.S. Department of Energy, under Contract No. DE-AC02-05CH11231. M.J.J. and Y.L. were also supported by the U.S. Department of Energy, Office of Science, Office of Basic Energy Sciences, Materials Sciences and Engineering Division, under Contract No. DE-AC02-05CH11231 within the Inorganic/Organic Nanocomposites Program (KC3104). A.W.-B. was supported by the U.S. Department of Energy Early Career Award. We thank Prof. Alexander Holleitner (Technical University Munich) and Prof. Ian Sharp (Technical University Munich) for insightful discussions.

REFERENCES

(1) Scholes, G. D.; Fleming, G. R.; Olaya-Castro, A.; van Grondelle, R. Lessons from Nature about Solar Light Harvesting. *Nat. Chem.* **2011**, *3*, 763−774.
(2) Piazza, F.; Sanejouand, Y.-H. Long-Range Energy Transfer in Proteins. *Phys. Biol.* **2009**, *6*, 046014.
(3) Pietryga, J. M.; Park, Y.-S.; Lim, J.; Fidler, A. F.; Bae, W. K.; Brovelli, S.; Klimov, V. I. Spectroscopic and Device Aspects of Nanocrystal Quantum Dots. *Chem. Rev.* **2016**, *116*, 10513−10622.
(4) Boles, M. A.; Ling, D.; Hyeon, T.; Talapin, D. V. The Surface Science of Nanocrystals. *Nat. Mater.* **2016**, *15*, 141−153.
(5) Kagan, C. R.; Lifshitz, E.; Sargent, E. H.; Talapin, D. V. Building Devices from Colloidal Quantum Dots. *Science* **2016**, *353*, aac5523.
(6) Lee, J.; Bao, W.; Ju, L.; Schuck, P. J.; Wang, F.; Weber-Bargioni, A. Switching Individual Quantum Dot Emission through Electrically Controlling Resonant Energy Transfer to Graphene. *Nano Lett.* **2014**, *14*, 7115−7119.
(7) Kholmicheva, N.; Moroz, P.; Eckard, H.; Jensen, G.; Zamkov, M. Energy Transfer in Quantum Dot Solids. *ACS Energy Lett.* **2017**, *2*, 154−160.
(8) Shaw, P. E.; Ruseckas, A.; Samuel, I. D. W. Exciton Diffusion Measurements in Poly(3-Hexylthiophene). *Adv. Mater.* **2008**, *20*, 3516−3520.
(9) Akselrod, G. M.; Prins, F.; Poulikakos, L. V.; Lee, E. M. Y.; Weidman, M. C.; Mork, A. J.; Willard, A. P.; Bulović, V.; Tisdale, W. A. Subdiffusive Exciton Transport in Quantum Dot Solids. *Nano Lett.* **2014**, *14*, 3556−3562.
(10) Yang, M.; Moroz, P.; Miller, E.; Porotnikov, D.; Cassidy, J.; Ellison, C.; Medvedeva, X.; Klinkova, A.; Zamkov, M. Energy Transport in $CsPbBr_3$ Perovskite Nanocrystal Solids. *ACS Photonics* **2020**, *7*, 154−164.
(11) Stranks, S. D.; Snaith, H. J. Metal-Halide Perovskites for Photovoltaic and Light-Emitting Devices. *Nat. Nanotechnol.* **2015**, *10*, 391−402.
(12) Curutchet, C.; Franceschetti, A.; Zunger, A.; Scholes, G. D. Examining Förster Energy Transfer for Semiconductor Nanocrystalline Quantum Dot Donors and Acceptors. *J. Phys. Chem. C* **2008**, *112*, 13336−13341.
(13) Kholmicheva, N.; Moroz, P.; Bastola, E.; Razgoniaeva, N.; Bocanegra, J.; Shaughnessy, M.; Porach, Z.; Khon, D.; Zamkov, M. Mapping the Exciton Diffusion in Semiconductor Nanocrystal Solids. *ACS Nano* **2015**, *9*, 2926.
(14) Mikhnenko, O. V.; Blom, P. W. M.; Nguyen, T.-Q. Exciton Diffusion in Organic Semiconductors. *Energy Environ. Sci.* **2015**, *8*, 1867−1888.
(15) Lunt, R. R.; Giebink, N. C.; Belak, A. A.; Benziger, J. B.; Forrest, S. R. Exciton Diffusion Lengths of Organic Semiconductor Thin Films Measured by Spectrally Resolved Photoluminescence Quenching. *J. Appl. Phys.* **2009**, *105*, 053711.
(16) Peumans, P.; Yakimov, A.; Forrest, S. R. Small Molecular Weight Organic Thin-Film Photodetectors and Solar Cells. *J. Appl. Phys.* **2003**, *93*, 3693−3723.
(17) Yang, L.-G.; Chen, H.-Z.; Wang, M. Optimal Film Thickness for Exciton Diffusion Length Measurement by Photocurrent Response in Organic Heterostructures. *Thin Solid Films* **2008**, *516*, 7701−7707.
(18) Brenner, T. M.; Egger, D. A.; Kronik, L.; Hodes, G.; Cahen, D. Hybrid Organic—Inorganic Perovskites: Low-Cost Semiconductors

with Intriguing Charge-Transport Properties. *Nat. Rev. Mater.* **2016**, *1*, 15007.
(19) Zhou, Y.; Zhu, K. Perovskite Solar Cells Shine in the "Valley of the Sun. *ACS Energy Lett.* **2016**, *1*, 64−67.
(20) Sutherland, B. R.; Sargent, E. H. Perovskite Photonic Sources. *Nat. Photonics* **2016**, *10*, 295−302.
(21) Kovalenko, M. V.; Protesescu, L.; Bodnarchuk, M. I. Properties and Potential Optoelectronic Applications of Lead Halide Perovskite Nanocrystals. *Science* **2017**, *358*, 745−750.
(22) Zheng, X.; Hou, Y.; Bao, C.; Yin, J.; Yuan, F.; Huang, Z.; Song, K.; Liu, J.; Troughton, J.; Gasparini, N.; Zhou, C.; Lin, Y.; Xue, D.-J.; Chen, B.; Johnston, A. K.; Wei, N.; Hedhili, M. N.; Wei, M.; Alsalloum, A. Y.; Maity, P. Managing Grains and Interfaces *via* Ligand Anchoring Enables 22.3%-Efficiency Inverted Perovskite Solar Cells. *Nat. Energy* **2020**, *5*, 131.
(23) Best Research-Cell Efficiencies. https://www.nrel.gov/pv/assets/pdfs/best-research-cell-efficiencies.20200406.pdf (accessed 05/19/2020).
(24) Lin, K.; Xing, J.; Quan, L. N.; de Arquer, F. P. G.; Gong, X.; Lu, J.; Xie, L.; Zhao, W.; Zhang, D.; Yan, C.; Li, W.; Liu, X.; Lu, Y.; Kirman, J.; Sargent, E. H.; Xiong, Q.; Wei, Z. Perovskite Light-Emitting Diodes with External Quantum Efficiency Exceeding 20 Per Cent. *Nature* **2018**, *562*, 245−248.
(25) Cao, Y.; Wang, N.; Tian, H.; Guo, J.; Wei, Y.; Chen, H.; Miao, Y.; Zou, W.; Pan, K.; He, Y.; Cao, H.; Ke, Y.; Xu, M.; Wang, Y.; Yang, M.; Du, K.; Fu, Z.; Kong, D.; Dai, D.; Jin, Y.; et al. Perovskite Light-Emitting Diodes-based on Spontaneously Formed Submicrometre-Scale Structures. *Nature* **2018**, *562*, 249−253.
(26) Park, M.-H.; Park, J.; Lee, J.; So, H. S.; Kim, H.; Jeong, S.-H.; Han, T.-H.; Wolf, C.; Lee, H.; Yoo, S.; Lee, T.-W. Efficient Perovskite Light-Emitting Diodes Using Polycrystalline Core-Shell-Mimicked Nanograins. *Adv. Funct. Mater.* **2019**, *29*, 1902017.
(27) Zhao, B.; Bai, S.; Kim, V.; Lamboll, R.; Shivanna, R.; Auras, F.; Richter, J. M.; Yang, L.; Dai, L.; Alsari, M.; She, X.-J.; Liang, L.; Zhang, J.; Lilliu, S.; Gao, P.; Snaith, H. J.; Wang, J.; Greenham, N. C.; Friend, R. H.; Di, D. High-Efficiency Perovskite-Polymer Bulk Heterostructure Light-Emitting Diodes. *Nat. Photonics* **2018**, *12*, 783−789.
(28) Protesescu, L.; Yakunin, S.; Bodnarchuk, M. I.; Krieg, F.; Caputo, R.; Hendon, C. H.; Yang, R. X.; Walsh, A.; Kovalenko, M. V. Nanocrystals of Cesium Lead Halide Perovskites ($CsPbX_3$, X = Cl, Br, and I): Novel Optoelectronic Materials Showing Bright Emission with Wide Color Gamut. *Nano Lett.* **2015**, *15*, 3692−3696.
(29) Swarnkar, A.; Marshall, A. R.; Sanehira, E. M.; Chernomordik, B. D.; Moore, D. T.; Christians, J. A.; Chakrabarti, T.; Luther, J. M. Quantum Dot-Induced Phase Stabilization of A-$CsPbI_3$ Perovskite for High-Efficiency Photovoltaics. *Science* **2016**, *354*, 92−95.
(30) Song, J.; Li, J.; Li, X.; Xu, L.; Dong, Y.; Zeng, H. Quantum Dot Light-Emitting Diodes Based on Inorganic Perovskite Cesium Lead Halides ($CsPbX_3$). *Adv. Mater.* **2015**, *27*, 7162−7167.
(31) Jellicoe, T. C.; Richter, J. M.; Glass, H. F. J.; Tabachnyk, M.; Brady, R.; Dutton, S. E.; Rao, A.; Friend, R. H.; Credgington, D.; Greenham, N. C.; Böhm, M. L. Synthesis and Optical Properties of Lead-Free Cesium Tin Halide Perovskite Nanocrystals. *J. Am. Chem. Soc.* **2016**, *138*, 2941−2944.
(32) Zhang, D.; Eaton, S. W.; Yu, Y.; Dou, L.; Yang, P. Solution-Phase Synthesis of Cesium Lead Halide Perovskite Nanowires. *J. Am. Chem. Soc.* **2015**, *137*, 9230−9233.
(33) Pan, A.; He, B.; Fan, X.; Liu, Z.; Urban, J. J.; Alivisatos, A. P.; He, L.; Liu, Y. Insight into the Ligand-Mediated Synthesis of Colloidal $CsPbBr_3$ Perovskite Nanocrystals: The Role of Organic Acid, Base, and Cesium Precursors. *ACS Nano* **2016**, *10*, 7943−7954.
(34) Shamsi, J.; Dang, Z.; Bianchini, P.; Canale, C.; Di Stasio, F. D.; Brescia, R.; Prato, M.; Manna, L. Colloidal Synthesis of Quantum Confined Single Crystal $CsPbBr_3$ Nanosheets with Lateral Size Control up to the Micrometer Range. *J. Am. Chem. Soc.* **2016**, *138*, 7240−7243.
(35) Imran, M.; Di Stasio, F.; Dang, Z.; Canale, C.; Khan, A. H.; Shamsi, J.; Brescia, R.; Prato, M.; Manna, L. Colloidal Synthesis of Strongly Fluorescent $CsPbBr_3$ Nanowires with Width Tunable Down to the Quantum Confinement Regime. *Chem. Mater.* **2016**, *28*, 6450−6454.
(36) Bekenstein, Y.; Koscher, B. A.; Eaton, S. W.; Yang, P.; Alivisatos, A. P. Highly Luminescent Colloidal Nanoplates of Perovskite Cesium Lead Halide and Their Oriented Assemblies. *J. Am. Chem. Soc.* **2015**, *137*, 16008−16011.
(37) Manzi, A.; Tong, Y.; Feucht, J.; Yao, E.-P.; Polavarapu, L.; Urban, A. S.; Feldmann, J. Resonantly Enhanced Multiple Exciton Generation through Below-Band-Gap Multi-Photon Absorption in Perovskite Nanocrystals. *Nat. Commun.* **2018**, *9*, 1518.
(38) Li, X.; Wu, Y.; Zhang, S.; Cai, B.; Gu, Y.; Song, J.; Zeng, H. $CsPbX_3$ Quantum Dots for Lighting and Displays: Room-Temperature Synthesis, Photoluminescence Superiorities, Underlying Origins and White Light-Emitting Diodes. *Adv. Funct. Mater.* **2016**, *26*, 2435−2445.
(39) Sun, S.; Yuan, D.; Xu, Y.; Wang, A.; Deng, Z. Ligand-Mediated Synthesis of Shape-Controlled Cesium Lead Halide Perovskite Nanocrystals *via* Reprecipitation Process at Room Temperature. *ACS Nano* **2016**, *10*, 3648−3657.
(40) Wei, S.; Yang, Y.; Kang, X.; Wang, L.; Huang, L.; Pan, D. Room-Temperature and Gram-Scale Synthesis of $CsPbX_3$ (X = Cl, Br, I) Perovskite Nanocrystals with 50−85% Photoluminescence Quantum Yields. *Chem. Commun.* **2016**, *52*, 7265−7268.
(41) Akkerman, Q. A.; Gandini, M.; Di Stasio, F.; Rastogi, P.; Palazon, F.; Bertoni, G.; Ball, J. M.; Prato, M.; Petrozza, A.; Manna, L. Strongly Emissive Perovskite Nanocrystal Inks for High-Voltage Solar Cells. *Nat. Energy* **2017**, *2*, 16194.
(42) Jurow, M. J.; Lampe, T.; Penzo, E.; Kang, J.; Koc, M. A.; Zechel, T.; Nett, Z.; Brady, M.; Wang, L.-W.; Alivisatos, A. P.; Cabrini, S.; Brütting, W.; Liu, Y. Tunable Anisotropic Photon Emission from Self-Organized $CsPbBr_3$ Perovskite Nanocrystals. *Nano Lett.* **2017**, *17*, 4534−4540.
(43) Xu, Y.; Chen, Q.; Zhang, C.; Wang, R.; Wu, H.; Zhang, X.; Xing, G.; Yu, W. W.; Wang, X.; Zhang, Y.; Xiao, M. Two-Photon-Pumped Perovskite Semiconductor Nanocrystal Lasers. *J. Am. Chem. Soc.* **2016**, *138*, 3761−3768.
(44) Loiudice, A.; Saris, S.; Oveisi, E.; Alexander, D. T. L.; Buonsanti, R. $CsPbBr_3$ QD/AlOx Inorganic Nanocomposites with Exceptional Stability in Water, Light, and Heat. *Angew. Chem., Int. Ed.* **2017**, *56*, 10696−10701.
(45) Moroz, P.; Kholmicheva, N.; Razgoniaeva, N.; Burchfield, D.; Sharma, N.; Acharya, A.; Zamkov, M. Optical Techniques for Probing the Excited State Dynamics of Quantum Dot Solids. *Chem. Phys.* **2016**, *471*, 59−68.
(46) Kagan, C. R.; Murray, C. B.; Nirmal, M.; Bawendi, M. G. Electronic Energy Transfer in Cdse Quantum Dot Solids. *Phys. Rev. Lett.* **1996**, *76*, 1517−1520.
(47) Crooker, S. A.; Hollingsworth, J. A.; Tretiak, S.; Klimov, V. I. Spectrally Resolved Dynamics of Energy Transfer in Quantum-Dot Assemblies: Towards Engineered Energy Flows in Artificial Materials. *Phys. Rev. Lett.* **2002**, *89*, 186802.
(48) Kennedy, C. L.; Hill, A. H.; Massaro, E. S.; Grumstrup, E. M. Ultrafast Excited-State Transport and Decay Dynamics in Cesium Lead Mixed Halide Perovskites. *ACS Energy Lett.* **2017**, *2*, 1501−1506.
(49) Guo, Z.; Manser, J. S.; Wan, Y.; Kamat, P. V.; Huang, L. Spatial and Temporal Imaging of Long-Range Charge Transport in Perovskite Thin Films by Ultrafast Microscopy. *Nat. Commun.* **2015**, *6*, 7471.
(50) Yoon, S. J.; Guo, Z.; dos Santos Claro, P. C.; Shevchenko, E. V.; Huang, L. Direct Imaging of Long-Range Exciton Transport in Quantum Dot Superlattices by Ultrafast Microscopy. *ACS Nano* **2016**, *10*, 7208−7215.
(51) Saris, S.; Loiudice, A.; Mensi, M.; Buonsanti, R. Exploring Energy Transfer in a Metal/Perovskite Nanocrystal Antenna to Drive Photocatalysis. *J. Phys. Chem. Lett.* **2019**, *10*, 7797−7803.